Applied Physics Letters

Mg-implanted bevel edge termination structure for GaN power device applications

Cite as: Appl. Phys. Lett. **118**, 093502 (2021); https://doi.org/10.1063/5.0039183
Submitted: 30 November 2020 • Accepted: 13 February 2021 • Published Online: 03 March 2021

Maciej Matys, Takashi Ishida, Kyung Pil Nam, et al.

ARTICLES YOU MAY BE INTERESTED IN

Formation of highly vertical trenches with rounded corners via inductively coupled plasma reactive ion etching for vertical GaN power devices
Applied Physics Letters **118**, 102101 (2021); https://doi.org/10.1063/5.0040920

Progress on and challenges of p-type formation for GaN power devices
Journal of Applied Physics **128**, 090901 (2020); https://doi.org/10.1063/5.0022198

High Mg activation in implanted GaN by high temperature and ultrahigh pressure annealing
Applied Physics Letters **118**, 022101 (2021); https://doi.org/10.1063/5.0038628

© 2021 Author(s).

Applied Physics Letters ARTICLE scitation.org/journal/apl

Mg-implanted bevel edge termination structure for GaN power device applications

Cite as: Appl. Phys. Lett. **118**, 093502 (2021); doi: 10.1063/5.0039183
Submitted: 30 November 2020 · Accepted: 13 February 2021 ·
Published Online: 3 March 2021

View Online

Export Citation
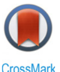
CrossMark

Maciej Matys,[1,a] Takashi Ishida,[1] Kyung Pil Nam,[1] Hideki Sakurai,[1,2] Tetsuo Narita,[3] Tsutomu Uesugi,[1] Michal Bockowski,[1,4] Jun Suda,[1] and Tetsu Kachi[1,a]

AFFILIATIONS

[1]Nagoya University, Nagoya 464-8601, Japan
[2]ATI, ULVAC, Inc., Chigasaki, Kanagawa 253-8543, Japan
[3]Toyota Central R&D Labs., Inc., Nagakute, Aichi 480-1192, Japan
[4]Institute of High Pressure Physics, Polish Academy of Sciences, Sokolowska 29/37, 01-142 Warsaw, Poland

[a]Authors to whom correspondence should be addressed: matys@imass.nagoya-u.ac.jp and kachi@imass.nagoya-u.ac.jp

ABSTRACT

Herein, we propose and demonstrate the edge termination for GaN-based one-sided abrupt p–n junctions. The structure is comprised of a combination of a shallow negative bevel mesa and selective-area p-type doping under the mesa. Based on the Technology Computer Aided Design (TCAD) simulation, the maximum electric field at the junction edge is markedly reduced to approximately 1.3 times that of the parallel-plane electric field in the proposed structure, which is almost half of the unimplanted diode. The TCAD simulation also shows that the shallow mesa angle of 6° effectively reduces the optimum acceptor concentration (N_a) in the implanted region and enhances the breakdown voltage. The optimum N_a value can be covered by the proposed technology based on the Mg-ion implantation and subsequent ultra-high-pressure annealing (UHPA). Using the formation of the shallow bevel mesa, the Mg-ion implantation, and the UHPA process, we experimentally demonstrate the p–n diodes with a breakdown voltage over 600 V, which is in good agreement with the TCAD simulation. The proposed method can be applied to a vertical trench-gate metal-oxide-semiconductor field-effect transistor with a high figure-of-merit.

Published under license by AIP Publishing. https://doi.org/10.1063/5.0039183

Over the last few years, we have witnessed the rapid evolution of GaN-based vertical devices, which has led to unprecedented progress in power technology.[1–7] Because of the unique vertical device architecture,[6–8] it has been possible to significantly improve the breakdown voltage (BV) and current density, which is difficult to realize in conventional lateral GaN high-electron mobility transistors or planar metal-oxide-semiconductor field-effect transistors (MOSFETs).[9–12]

For vertical power devices, one of the most important issues is the optimization of the electric field distribution because the electric field crowding at the device edges significantly reduces BV. To address this problem, various edge termination structures were developed, including field-limiting guard rings or junction termination extensions (JTEs). These edge termination structures are well known for Si- or SiC-based devices, but it is difficult to apply such technology for GaN-based devices owing to the inefficiency of selective-area p-type doping (below 10%).[13–16] Therefore, various groups proposed an alternate junction termination method for GaN such as a moat etch termination,[17] vertically and deeply etched mesa structure,[18] hydrogen plasma-based structure,[19] and field plate combined with a p-type punch-through structure.[20] Such methods do not require selective area doping, but they need the specific designs and/or complex technological processes. Therefore, realization of ion-implanted edge termination structures for GaN would drastically improve the flexibility of GaN-based devices and would be a crucial step for future GaN power electronics.

A trench-gate MOSFET has the advantage of reducing the low on-state resistance by reducing the cell pitch.[3,21–26] In this structure, the electric field crowding is caused at the edge of the p–n junction, which consists of a p-type body layer with the acceptor concentration (N_A) around 10^{18} cm^{-3} and an n-type drift layer with the donor concentration (N_D) around 10^{16} cm^{-3} to obtain a high BV. In such a one-side abrupt p–n junction with a large N_A/N_D ratio, the simple bevel mesa edge termination structure does not work for the electric field relaxation.[27–29] The combination with a selective area p-type doping has been one of the effective approaches to reduce the electric field concentration in this structure if the sufficient acceptor concentration is obtained in the Mg-ion-implanted region.

Recently, our group achieved a high acceptor activation ratio of Mg-ion-implanted GaN using an ultra-high-pressure annealing

Published under license by AIP Publishing

(UHPA) process.[30,31] This technology is based on the high-temperature annealing under 1 GPa over the equilibrium partial N_2 pressure in the phase diagram of GaN-Ga-N_2, which allows annealing without a surface degradation.[32] In this study, we design the edge termination structure combining a shallow bevel mesa with a selective-area doping for the p–n junction with a large N_A/N_D ratio of approximately 100 based on the TCAD simulations [see Fig. 1(a)]. We also experimentally demonstrate BV enhancements for the proposed diodes processed through the UHPA technique, which is consistent with the TCAD simulations assuming acceptor activation ratios of over 70%.

In the first step, we theoretically estimated the impact of Mg implantation on BV for the bevel edge termination structure by means of TCAD simulations implemented in Synopsys Software. In the simulations, we used the impact ionization coefficients experimentally extracted from the above- and sub-bandgap illuminations for a GaN-based p–/n+ junction.[33] Figure 1(a) shows the GaN-based bevel structure used in the simulations. The layered structure was designed in the following bottom-to-top order: 7 μm-thick n-type GaN drift layer (effective donor concentration of 2×10^{16} cm^{-3}), 0.5 μm-thick p-type GaN layer (2×10^{18} cm^{-3}), and 0.1 μm-thick p+GaN layer (5×10^{19} cm^{-3}). The depth of the mesa was 1.5 μm, and the additionally implanted p-GaN region was placed on the beveled area across the boundary between the original p-GaN layer and the n-type drift layer [see Fig. 1(a)].

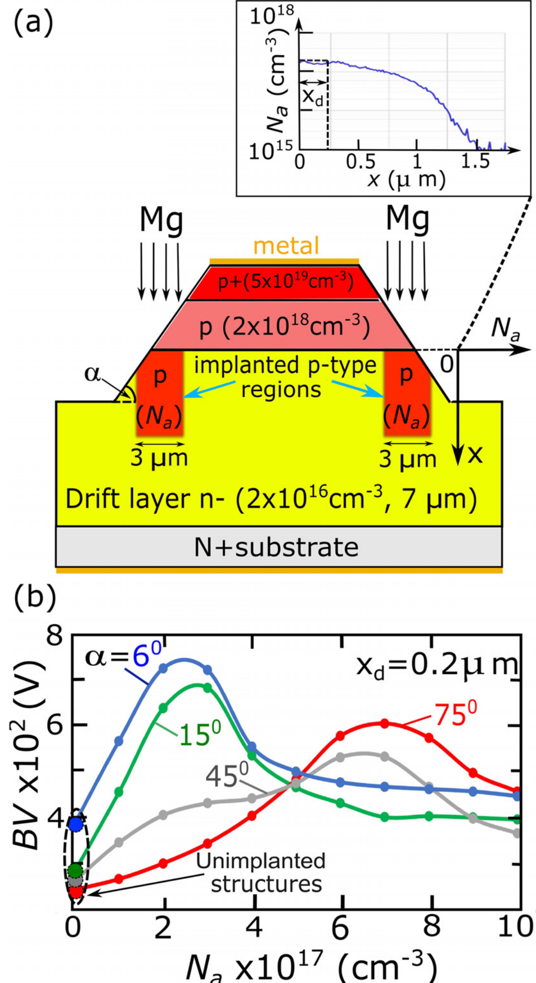

FIG. 1. Schematic of the beveled-mesa structure with the implanted p-type region (a) and calculated dependencies of the breakdown voltage on the acceptor concentration (N_a) of the implanted p-type region at $x = 0$ in the case of $\alpha = 6°$, 15°, 45°, and 75° (b). The inset in Fig. 1(a) shows the N_a depth distribution (according to the SIMS profile of Mg ions obtained in the UHPA process) assumed in the calculations.

Figure 1(b) shows the calculated BV as a function of the acceptor concentration (N_a) of the implanted p-type region. In the calculations, we assumed the N_a depth distribution based on the depth profile of Mg atoms after the UHPA process reported previously[30,31] [see the inset of Fig. 1(a)]. The simulations were conducted for different bevel angles, that is, $\alpha = 6°$, 15°, 45°, and 75°. We found that there is an optimal N_a value for each mesa angle α. The maximum BV for $\alpha = 6°$ is higher than that for $\alpha = 15°$, 45°, and 75°.

To understand this trend, in Figs. 2(a)–2(c), we present the cross-sectional electric field distribution in the device (at $\alpha = 6°$) under BV conditions, where the electric field (E) reaches a critical value of GaN.[27] Note that the structure without the implanted p-type region, i.e., $N_a = 0$, exhibits a highly concentrated electric field at the p–n junction near the bevel surface [see Fig. 2(a)], which strongly limits BV to 401 V. In contrast, in the case of the optimum doping level, corresponding to an N_a value of 2×10^{17} cm^{-3}, the electric field becomes relaxed, i.e., the electric field exhibits two maxima: the first one is located at the p–n junction (close to the bevel surface) and the second inside the implanted p-type region [Fig. 2(b)]. Such a distribution of the electric field leads to a remarkable increase in BV up to 730 V [see Fig. 2(b)]. When N_a is significantly high, for example, reaches 5×10^{17} cm^{-3} [see Fig. 2(c)], the electric field becomes strongly localized at the outer border in the implanted region, and therefore, BV is significantly reduced to 513 V [Fig. 2(c)]. Figure 2(d) plots the electric field distribution normalized by the parallel-plane electric field (E_{PP}) along the p–n junction defined as:[27] $E_{PP} = \sqrt{\frac{2e(V_d - BV)N_A \cdot N_D}{\varepsilon_s(N_A + N_D)}}$, where V_d and ε_s are the built-in potential and dielectric constant, respectively. For the optimal $N_a = 2 \times 10^{17}$ cm^{-3}, the maximum electric field (E_{max}) is approximately 1.3 times higher than that of the parallel-plane field (E_{PP}), whereas the maximum field reaches 2.2 times of E_{PP} in the unimplanted diodes, as shown in Fig. 2(d). Note that the optimal N_a value is reduced for the shallower α, as shown in Fig. 1(b). It should be emphasized that the optimal $N_a = 2 \times 10^{17}$ cm^{-3} for $\alpha = 6°$ is available in the present Mg-ion implantation technology using UHPA.[30,31] Moreover, the BV value increases with the decreasing bevel angle owing to the electric field relaxation via the shallow bevel. Thus, we can design an effective edge termination by combining the shallow bevel with selective-area p-type doping. To remove the remaining electric field crowding in the optimal condition in Fig. 2(b), the application of an additional outer p-region such as JTE is necessary.

Next, the impact of the N_a vertical depth profile on BV was investigated (the impact of the lateral width of the implanted p-type region on BV can be negligible (see the supplementary material]. Here, the addition of the box-shaped region with a depth of x_d to the optimal condition in Fig. 1(b) was assumed to be constant and equal to 2×10^{17} cm^{-3}, while the profile below the box region was based on

Published under license by AIP Publishing

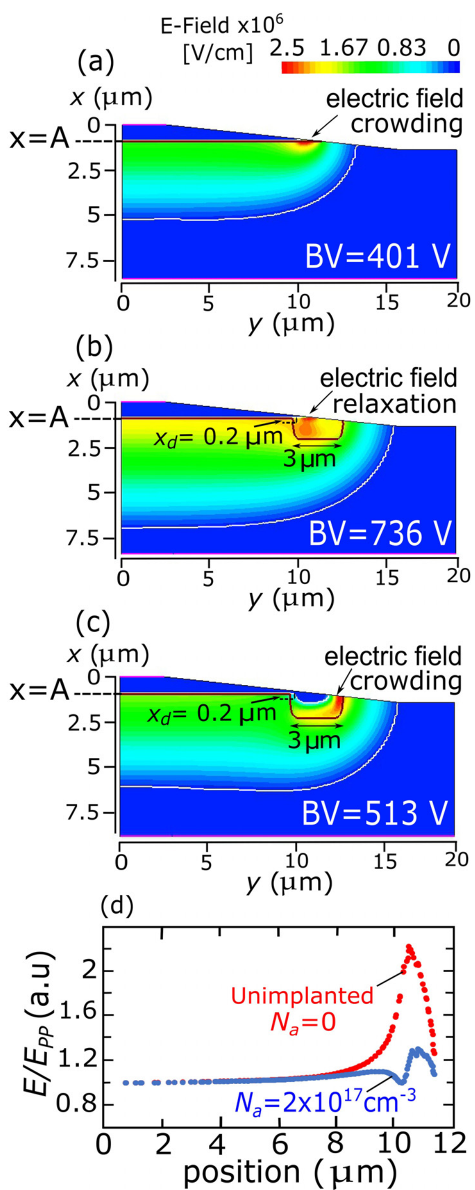

FIG. 2. Two-dimensional electric field distribution in the beveled-mesa structure: without p-type region $N_a = 0$ (a), $N_a = 2 \times 10^{17}$ cm^{-3} (b), and $N_a = 5 \times 10^{17}$ cm^{-3} (c). The line at $x = 0$ indicates the p–n junction interface. Figure 3(d) shows the electric field distribution along the x = A line normalized to the parallel-plane peak field, E_{PP}.

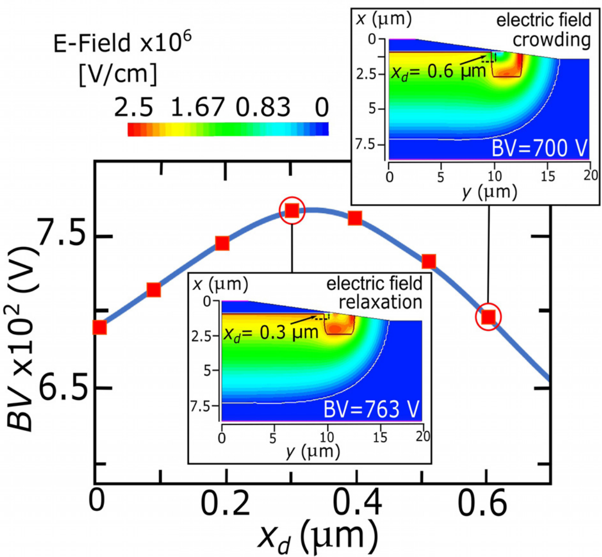

FIG. 3. Calculated dependencies of BV as a function of x_d parameter. The insets of Fig. 3 show the electric field distribution in the case of $x_d = 0.3\,\mu$m and $x_d = 0.6\,\mu$m. The brown line in the electric field distribution indicates the p–n junction. Note that the shape of the bottom corner of the p–n junction changes markedly with the increasing x_d parameter. This is due to the deeper location of the p–n junction with increasing x_d.

the homologous shape of the Mg diffusion profile obtained from the previous experiment.[30,31] Note that when $x_d = 0.2\,\mu$m, the N_a depth profile was the same as that in the inset of Fig. 1(a). The simulations were performed for the bevel angle of $\alpha = 6°$. Figure 3 shows the calculated BV as a function of x_d. Note that there exists an optimal x_d value for which a high BV can be realized. For $x_d = 0$, the electric field exhibits only two peaks, as shown in Fig. 2(b), where the electric concentration near the surface is higher than that of the bottom peak. For an excessively large x_d (for example, $x_d = 0.6\,\mu$m), the electric field is significantly concentrated at the outer border in the implanted region, as shown in the inset of Fig. 3, resulting in a reduction of BV to 700 V. For the optimal condition of $x_d = 0.3\,\mu$m, the electric field concentration is equally distributed to the bevel surface and the outer border, as seen in the inset of Fig. 3, which results in the highest BV of 763 V. Therefore, by optimizing the depth of the box-shaped region x_d, it is possible to improve BV.

To experimentally demonstrate the simulated edge termination, we fabricated vertical p–n diodes with Mg-implanted bevel edge termination annealed through the UHPA process.[30,31] The layered structure of a p–n diode was grown by metalorganic vapor phase epitaxy on a free standing n-type GaN (0001) substrate and was composed of a 7-μm-thick n-GaN drift layer doped with silicon, a 0.45-μm-thick p-GaN layer doped with an Mg concentration of 2×10^{18} cm^{-3}, and a 0.1-μm-thick p$^+$-GaN layer doped with an Mg concentration of 10^{19} cm^{-3} as obtained from the SIMS profile. The effective donor concentration of the drift layer was estimated to be 2.4×10^{16} cm^{-3} by capacitance–voltage (C–V) measurements. The compensation ratio of the drift layer was estimated from SIMS measurements as [C]/[Si] = 0.15, where [Si] = 2×10^{16} cm^{-3}. The bevel mesa is formed by the thermal reflow process of the photoresist and the subsequent Cl_2-based inductively coupled plasma reactive ion etching.[27] The optimized process allowed for the formation of a shallow bevel angle of around 6° with the standard deviation of +/-1°. The BV changes corresponding to such variations of the bevel angle are equal to 50 V according to TCAD simulations (see the supplementary material). Next, the Mg ions were implanted at room temperature with ion energies of 20, 45, 90, 150, 240, and 430 keV and dosages, where two diodes with different total dosages were prepared, as summarized in Table I. It should be noted that the Mg implantation process was performed

TABLE I. Summary of Mg-ion implantation conditions used in two p–n diodes. Mg ions were implanted using multiple energies to obtain 0.4 μm-depth box shape profiles.

Energy (keV)	Mg dosage I (cm^{-2})	Mg dosage II (cm^{-2})
20	3.5×10^{11}	5.8×10^{11}
45	8×10^{11}	1.3×10^{12}
90	1.5×10^{12}	2.5×10^{12}
150	2.2×10^{12}	3.7×10^{12}
240	4×10^{12}	6.7×10^{12}
430	1.1×10^{13}	1.8×10^{13}
Total	2×10^{13}	3.3×10^{13}

without using a protection film of the GaN surface. Subsequently, we conducted UHPA under an N_2 pressure of 1 GPa at a temperature of 1400 °C for 15 min. Details of the UHPA process can be found in Refs. 22 and 23. Figure 4 shows the Mg profile estimated by SIMS after the activation and diffusion of Mg atoms through the UHPA process. From this figure, we estimated the width of the Mg box profile to be 0.4 μm and the average Mg concentration to be 3×10^{17} cm^{-3} (sample I) and 5×10^{17} cm^{-3} (sample II). In this context, it should be emphasized that the Mg concentration in the lateral direction has a similar distribution as in an epitaxially grown layer. This is a quite different situation from that in the vertical direction case where the Mg distribution is strongly determined by the defect-enhanced diffusion process.[7,31] Essentially, the Ni/Au and Ti/Al/Ni/Au metal contacts were deposited on the p^+ GaN layer and substrate, respectively. More details about the fabrication process of the beveled-mesa structure can be found in Refs. 27 and 33. No surface degradation was observed in the fabricated diodes as optical microscopy showed.

Subsequently, the reverse current–voltage (I–V) measurements were carried without using the fluorinert medium. Based on the examination of the large number of diodes, BV values of unimplanted diodes were limited to 450 ± 40 V, as shown by the red solid line in Fig. 5. For Diodes I and II with Mg-implanted termination, the BV values were significantly enhanced up to 650 V ± 50 V (see Fig. 5). Furthermore, the leakage currents were drastically reduced in the Mg-implanted diodes. Moreover, for comparison, we prepared the bevel structures with SiO_2 surface passivation. However, we did not observe

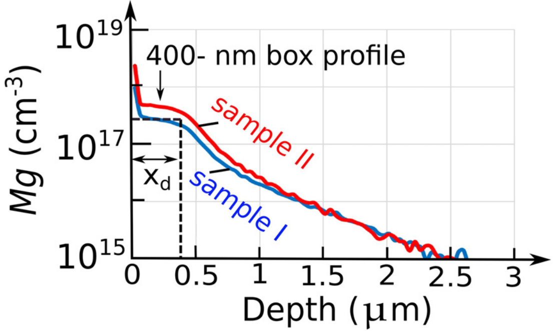

FIG. 4. 0.4 μm box profile of Mg concentrations obtained from SIMS for samples I and II.

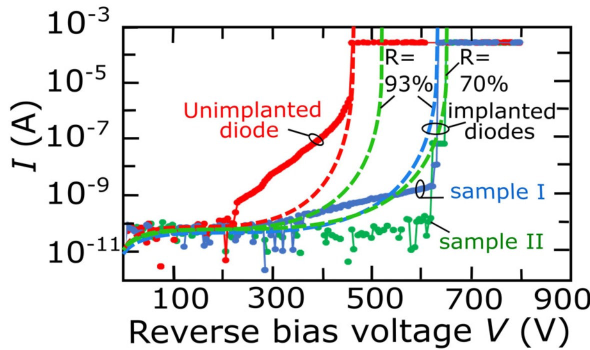

FIG. 5. Experimental (points) and theoretical (dashed lines) reverse *I–V* characteristics for unimplanted and implanted bevel diodes. Theoretical curves for implanted diodes were calculated assuming R = 93% (samples I and II) and R = 70% (sample II).

any significant effect of SiO_2 passivation on BV. The improvement in BV due to Mg implantation is in accordance with the simulation predictions [Fig. 1(b)], although there was little difference in BV for different Mg concentrations between samples I and II.

To understand these results, we calculated the *I-V* characteristics of the fabricated diodes and compared them with the experimental ones, as shown in Fig. 5. In the simulations, we assumed the N_a depth profiles according to the Mg SIMS profile shown in Fig. 4 (to obtain the N_a profile, we multiplied the Mg depth profile from Fig. 4 by the R factor, which is the activation ratio of Mg in the UHPA process, $N_a = R \cdot [Mg]$). First, it should be noted that the I-V curves cannot be fitted using the same R value for both samples. For example, assuming R = 93% (the best fitted value for sample I), we obtained that sample II should exhibit a BV of 526 V, as shown in Fig. 5, which is much lower value than that experimentally observed (650 V). This fact results directly from the trend shown in Fig. 1(b). Namely, sample II has [Mg] = 5×10^{17} cm^{-3} (see Fig. 4), and thus assuming R ≈ 100%, we have from Fig. 1(b) BV ≈ 500 V (for $N_a \approx 5 \times 10^{17}$ cm^{-3}). On the other hand, the measured I-V characteristics can be well reproduced by the calculated ones for both the unimplanted and implanted diodes if we assume different R values between samples I and II, i.e., for sample I, R = 93% and for sample II, R = 70%. It should be noted that the R value is determined by the compensation via donor-like defects (N_d), which can be introduced by the ion implantation damage [Mg]. Due to this fact, the acceptor concentration N_a should be expressed as $N_a = R \cdot [Mg] - N_d \approx R^* Mg$, where R^* is the effective R factor, which involves N_d. At present, we cannot separate the N_d value from N_a. However, our previous study indicated that the N_d/N_a value was in the range from 10% to 30%.[30,31,34] Since the N_d value can be increased by the higher implantation dosage [Mg], this explains the lower R^* value for sample II (70%) compared to sample I (93%). This also means that both samples can have a very similar N_a value (in Sample I: $N_a = 0.93 \times 3 \times 10^{17}$ $cm^{-3} = 2.8 \times 10^{17}$ cm^{-3} and in sample II: $N_a = 0.7 \times 5 \times 10^{17}$ $cm^{-3} = 3.5 \times 10^{17}$ cm^{-3}), which clarifies why we did not observe a strong dependence of BV on N_a. Furthermore, the ideal BV for a one-side abrupt p–n junction with $N_D = 2.4 \times 10^{16}$ cm^{-3} is estimated to be 842 V.[27] Therefore, the ratio E_{max}/E_{PP} for implanted diodes can be roughly estimated to be 842 V/(650 ± 50) V = 1.2 ∼ 1.4, while that for unimplanted diodes is 842 V/(450 ± 50) V = 1.7 ∼ 2.1.

Published under license by AIP Publishing

This is consistent with the theoretical calculations of the electric field distribution along the p–n junction [see Fig. 2(d)], which supports the accuracy of our analysis.

Finally, it should be highlighted that our analysis is based on the assumption that the breakdown occurs mainly due to the impact ionization process. In order to support this assumption, we performed the temperature-dependent reverse-bias I–V measurements for the Mg-implanted diode (see Fig. S3 in the supplementary material). We observed a shift of BV toward higher voltages with temperature, which can be a signature of the avalanche breakdown. Nevertheless, we cannot entirely exclude other possible causes of the breakdown like, for example, V-shaped defects (pits).

In conclusion, we designed, fabricated, and characterized the one-side abrupt p–n junction diodes with Mg-implanted shallow bevel edge termination for high-power device applications. The TCAD simulations showed that the optimization of the acceptor concentration and effective depth in the implanted region effectively suppresses the electric field crowding at the bevel mesa edge. Furthermore, the shallow bevel angle reduced the optimal acceptor concentration to the level that was available in the present Mg-ion implantation technology based on the UHPA process. The diodes with Mg-implanted bevel terminations enhanced the breakdown voltage and suppressed the leakage current compared with the unimplanted diodes, indicating effective electric field relaxation. Assuming an Mg activation ratio of more than 70% in the implanted region, TCAD simulations reproduced the reverse bias characteristics obtained from the experiment. The highly effective selective-area p-type doping in the bevel mesa structure is a crucial step for future GaN power electronic devices.

See the supplementary material for the additional analysis of the impact of the standard deviation of the bevel angle of 6° and the lateral width of the implanted p-type region on BV of the bevel structure and temperature-dependent I–V characteristics of the Mg-implanted diode.

This work was supported by MEXT "Research and development of next-generation semiconductor to realize energy-saving society Program Grant No. JPJ005357. Part of this research was also supported by the Polish National Science Centre through Project No. 2018/29/B/ST5/00338. M.M. expresses gratitude to Professor Tamotsu Hashizume (RCIQE) for his kind support and discussions.

DATA AVAILABILITY

The data that support the findings of this study are available from the corresponding author upon reasonable request.

REFERENCES

[1] H. Nie, Q. Diduck, B. Alvarez, A. P. Edwards, B. M. Kayes, M. Zhang, G. Ye, T. Prunty, D. Bour, and I. C. Kizilyalli, IEEE Electron Device Lett. **35**, 939–941 (2014).
[2] D. Shibata, R. Kajitani, M. Ogawa, K. Tanaka, S. Tamura, T. Hatsuda, M. Ishida, and T. Ueda, in *IEEE International Electron Devices Meeting (IEDM)* (IEEE, 2016), p. 248.
[3] T. Oka, T. Ina, Y. Ueno, and J. Nishii, Appl. Phys. Express **8**, 054101 (2015).
[4] R. Tanaka, S. Takashima, K. Ueno, H. Matsuyama, and M. Edo, Jpn. J. Appl. Phys., Part 1 **59**, SGGD02 (2020).
[5] H. Amano, Y. Baines, E. Beam, M. Borga, T. Bouchet, P. R. Chalker, M. Charles, K. J. Chen, N. Chowdhury, R. Chu, C. De Santi, M. M. De Souza, S. Decoutere, L. D. Cioccio, B. Eckardt, T. Egawa, P. Fay, J. J. Freedsman, L. Guido, O. Häberlen, G. Haynes, T. Heckel, D. Hemakumara, P. Houston, J. Hu, M. Hua, Q. Huang, A. Huang, S. Jiang, H. Kawai, D. Kinzer, M. Kuball, A. Kumar, K. B. Lee, X. Li, D. Marcon, M. März, R. McCarthy, G. Meneghesso, M. Meneghini, E. Morvan, A. Nakajima, E. M. S. Narayanan, S. Oliver, T. Palacios, D. Piedra, M. Plissonnier, R. Reddy, M. Sun, I. Thayne, A. Torres, N. Trivellin, V. Unni, M. J. Uren, M. Van Hove, D. J. Wallis, J. Wang, J. Xie, S. Yagi, S. Yang, C. Youtsey, R. Yu, E. Zanoni, S. Zeltner, and Y. Zhang, J. Phys. D: Appl. Phys. **51**, 163001 (2018).
[6] T. Kachi, Jpn. J. Appl. Phys., Part 1 **53**(10), 100210–100211 (2014).
[7] T. Narita, H. Yoshida, K. Tomita, K. Kataoka, H. Sakurai, M. Horita, M. Bockowski, N. Ikarashi, J. Suda, T. Kachi, and Y. Tokuda, J. Appl. Phys. **128**, 090901 (2020).
[8] I. C. Kizilyalli, A. P. Edwards, O. Aktas, T. Prunty, and D. Bour, IEEE Trans. Electron Devices **62**, 414 (2015).
[9] T. Hashizume, K. Nishiguchi, S. Kaneki, J. Kuzmik, and Z. Yatabe, Mater. Sci. Semicond. Process. **78**, 85–95 (2018).
[10] Z. Yatabe, J. Asubar, and T. Hashizume, J. Phys. D: Appl. Phys. **49**, 393001 (2016).
[11] U. K. Mishra, L. Shen, T. E. Kazior, and Y. F. Wu, Proc. IEEE **96**, 287 (2008).
[12] T. Ueda, M. Ishida, T. Tanaka, and D. Ueda, Jpn. J. Appl. Phys., Part 1 **53**, 100214 (2014).
[13] A. M. Ozbek and B. J. Baliga, IEEE Electron Device Lett. **32**, 300 (2011).
[14] J. J. Wierer, J. R. Dickerson, A. A. Allerman, A. M. Armstrong, M. H. Crawford, and R. J. Kaplar, IEEE Trans. Electron Devices **64**(5), 2291 (2017).
[15] T. Niwa, T. Fujii, and T. Oka, Appl. Phys. Express **10**, 091002 (2017).
[16] T. J. Anderson, B. N. Feigelson, F. J. Kub, M. J. Tadjer, K. D. Hobart, M. A. Mastro, J. K. Hite, and C. R. Eddy, Jr., Electro. Lett **50**, 197 (2014).
[17] D. Ji, S. Li, B. Ercan, C. Ren, and S. Chowdhury, IEEE Electron Device Lett. **41**, 264–267 (2020).
[18] H. Fukushima, S. Usami, Y. Ando, A. Tanaka, M. Deki, M. Kushimoto, S. Nitta, Y. Honda, and H. Amano, Appl. Phys. Express **12**, 026502 (2019).
[19] H. Fu, K. Fu, X. Huang, H. Chen, I. Baranowski, T.-H. Yang, J. Montes, and Y. Zhao, IEEE Electron Device Lett. **39**, 1018 (2018).
[20] H. Ohta, N. Asai, F. Horikiri, Y. Narita, T. Yoshida, and T. Mishima, Jpn. J. Appl. Phys., Part 1 **58**, SCCD03 (2019).
[21] D. Ji, C. Gupta, S. H. Chan, A. Agarwal, W. Li, S. Keller, U. K. Mishra, and S. Chowdhury, in IEEE International Electron Devices Meeting, Technical Digest (2017), p. 9.4.1.
[22] C. Gupta, S. H. Chan, A. Agarwal, N. Hatui, S. Keller, and U. K. Mishra, IEEE Electron Device Lett. **38**, 1575 (2017).
[23] D. Ji, A. Agarwal, H. Li, W. Li, S. Keller, and S. Chowdhury, IEEE Electron Device Lett. **39**, 863 (2018).
[24] M. Kodama, M. Sugimoto, E. Hayashi, N. Soejima, O. Ishiguro, M. Kanechika, K. Itoh, H. Ueda, T. Uesugi, and T. Kachi, Appl. Phys. Express **1**, 021104 (2008).
[25] R. Li, Y. Cao, M. Chen, and R. Chu, IEEE Electron Device Lett. **37**, 1466 (2016).
[26] T. Ishida, K. Pil Nam, M. Matys, T. Uesugi, J. Suda, and T. Kachi, Appl. Phys. Express **13**, 124003 (2020).
[27] T. Maeda, T. Narita, H. Ueda, M. Kanechika, T. Uesugi, T. Kachi, T. Kimoto, M. Horita, and J. Suda, IEEE Electron Device Lett. **40**, 941 (2019).
[28] A. T. Binder, J. R. Dickerson, M. H. Crawford, G. W. Pickrell, A. A. Allerman, P. Sharps, and R. J. Kaplar, in IEEE 7th Workshop on Wide Bandgap Power Devices and Applications (WiPDA), Raleigh, NC, USA (2019), pp. 281–285.
[29] K. Zeng and S. Chowdhury, IEEE Trans. Electron Devices **67**, 2457 (2020).
[30] H. Sakurai, M. Omori, S. Yamada, Y. Furukawa, H. Suzuki, T. Narita, K. Kataoka, M. Horita, M. Bockowski, J. Suda, and T. Kachi, Appl. Phys. Lett. **115**, 142104 (2019).
[31] H. Sakurai, T. Narita, M. Omori, S. Yamada, A. Koura, M. Iwinska, K. Kataoka, M. Horita, N. Ikarashi, M. Bockowski, J. Suda, and T. Kachi, Appl. Phys. Express **13**, 086501 (2020).
[32] K. Sierakowski, R. Jakiela, B. Lucznik, P. Kwiatkowski, M. Iwinska, M. Turek, H. Sakurai, T. Kachi, and M. Bockowski, Electronics **9**, 1380 (2020).
[33] T. Maeda, T. Narita, S. Yamada, T. Kachi, T. Kimoto, and M. Horita, in IEEE International Electron Devices Meeting, Technical Digest (2019), pp. 4.2.1–4.2.4.
[34] K. Kataoka, T. Narita, H. Iguchi, T. Uesugi, and T. Kachi, Phys. Status. Solidi B **255**, 1700379 (2018).

Published under license by AIP Publishing